Potential Vorticity Diagnosis of the Factors Affecting the Track of Typhoon Sinlaku (2008) and the Impact from Dropwindsonde Data during T-PARC

CHUN-CHIEH WU, SHIN-GAN CHEN, CHUNG-CHUAN YANG, AND PO-HSIUNG LIN

Department of Atmospheric Sciences, National Taiwan University, Taipei, Taiwan

SIM D. ABERSON

NOAA/AOML/Hurricane Research Division, Miami, Florida

(Manuscript received 9 September 2011, in final form 11 February 2012)

ABSTRACT

In 2008, abundant dropwindsonde data were collected during both reconnaissance and surveillance flights in and around tropical cyclones (TCs) in the western North Pacific basin under the framework of The Observing System Research and Predictability Experiment (THORPEX)–Pacific Asian Regional Campaign (T-PARC). The National Centers for Environmental Prediction Global Forecast System (GFS) showed significant track improvements for Typhoon Sinlaku (2008) after the assimilation of dropwindsonde data. For this particular typhoon, the potential vorticity (PV) diagnosis is adopted to understand the key factors affecting the track. A data denial run initialized at 0000 UTC 10 September is examined to evaluate how the extra data collected during T-PARC improve GFS track forecasts.

A quantitative analysis of the steering flow based on the PV diagnosis indicates that the Pacific subtropical high to the east of Sinlaku is a primary factor that advects Sinlaku northwestward, while the monsoon trough plays a secondary role. The assimilation of dropwindsonde data improves the structure and intensity of the initial vortex and maintains the forecast vortex structure in the vertical. The difference in the vertical extent of the vortices could be regarded as a cause for the discrepancy in steering flow between runs with and without the dropwindsonde data. This paper highlights the importance of improved analyses of the vertical TC structure, and thus of a representative steering flow in the deep troposphere during the forecasts.

1. Introduction

Tropical cyclones (TCs) in the western North Pacific basin often move westward or northwestward, due to the predominant steering flow associated with the Pacific subtropical high. However, during the late season, TCs may slow, stall, or recurve near 130°E because of the weakening of the subtropical high, the strengthening of the continental high over China, and/or the presence of a deep midlatitude baroclinic wave/trough (Wu et al. 2004). In addition, unusual TC motion, such as an abrupt northward turn, may occur because of the TC interacting with a low-latitude monsoon trough (Lander 1996). Other features that affect TC motion include upper-level cold-core lows and other TCs (binary interaction; Wu et al. 2003). In all, the environmental flow across a TC is generally a combination of the flows associated with any of the above features. The complicated interactions between these features often result in large track forecast errors as numerical models sometimes fail to represent them well.

Inaccurate initial and boundary conditions in numerical models are primarily due to the scarcity of observational data around TCs in the open ocean, often leading to poor track and intensity forecasts (Wu and Kuo 1999). Following the success of hurricane surveillance in the Atlantic (Aberson and Franklin 1999; Aberson 2002), the Dropwindsonde Observations for Typhoon Surveillance near the Taiwan Region (DOTSTAR) program began a new era of TC surveillance and targeted observations in the western North Pacific in 2003 (Wu et al. 2005). Through 2011, 55 surveillance missions have been conducted around 42 TCs, with 905 dropwindsondes deployed. Particularly, in the summer of 2008, DOTSTAR participated in the international field campaign of The Observing System Research and Predictability Experiment

Corresponding author address: Dr. Chun-Chieh Wu, Dept. of Atmospheric Sciences, National Taiwan University, No. 1, Sec. 4, Roosevelt Rd., Taipei 106, Taiwan.
E-mail: cwu@typhoon.as.ntu.edu.tw

DOI: 10.1175/MWR-D-11-00229.1

(THORPEX)–Pacific Asian Regional Campaign (T-PARC), collaborating with the Tropical Cyclone Structure 2008 (TCS-08) and Typhoon Hunting 2008 (TH08) experiments. A wide variety of observational airborne platforms, including the U.S. Air Force WC-130J with the Stepped Frequency Microwave Radiometer (SFMR), the U.S. Navy P-3 with the Electra Doppler Radar (ELDORA) and a Doppler wind lidar, the DOTSTAR Astra jet with dropwindsondes, and the DLR Falcon, were used to observe TCs in the western North Pacific basin. Based on different aircraft functions, the WC-130J and P-3 conducted reconnaissance flights gathering observations in the TC core and rainbands, and the Astra and Falcon were responsible for observations around the TC and in sensitive (targeted) areas. This was the first time that four aircraft were simultaneously operated in the western North Pacific, and they collected unprecedented and valuable data during the entire TC life cycle. Research studies on such topics as genesis, intensity and structure changes, recurvature, observation targeting, extratropical transition, and their downstream impacts are ongoing (Elsberry and Harr 2008). Additionally, drifting buoys and other in situ instruments were launched from various platforms.

One of the key components of T-PARC is the further exploration of targeted observations as addressed in a series of papers (e.g., Wu 2006; Wu et al. 2007a, 2009a,b,c; Chen et al. 2009; Yamaguchi et al. 2009; Aberson et al. 2011; Chen et al. 2011; Majumdar et al. 2011). Dropwindsonde data were not only transmitted in real time to operational centers such as the Central Weather Bureau (CWB) of Taiwan, the National Centers for Environmental Prediction (NCEP), and the Japan Meteorological Agency (JMA), and were also used to assess their impact on model forecasts. The dropwindsonde data improved the mean model track forecasts by 15%–40% (Aberson 2003, 2011; Wu et al. 2007b; Chou et al. 2011; Harnisch and Weissmann 2010; Weissmann et al. 2011). Nevertheless, it is shown that the impact of the dropwindsonde data is dependent on the modeling systems; for example, the impact on the European Centre for Medium-Range Weather Forecasts (ECMWF) model is not statistically significant, unlike in the NCEP model, likely due to the better performance of the ECMWF system with more extensive use of satellite data and four-dimensional variational data assimilation (4D-Var; Chou et al. 2011; Weissmann et al. 2011). Assimilation of dropwindsonde data near the TC core into the numerical models may lead to forecast degradation in some cases (Aberson 2008; Weissmann et al. 2011). More recently, dropwindsonde data collected during T-PARC have been used to evaluate the impact of the observation based on the ensemble sensitivity derived by the local ensemble transform Kalman filter (LETKF) in the Weather Research and Forecasting Model (WRF) (Kunii et al. 2012). Further analysis is needed to evaluate impacts of specific data between different modeling systems. In addition to the impact on the TC track forecast, several interesting scientific issues related to the TC intensity and structure change have also been explored using dropwindsonde data, such as dynamical processes of concentric eyewall formation (Huang et al. 2012; Wu et al. 2012) based on the ensemble Kalman filter (EnKF; Zhang et al. 2006; Wu et al. 2010).

Typhoon Sinlaku (2008) had the largest number of dropwindsondes deployed during T-PARC. Chou et al. (2011) showed significant track forecast improvement in the NCEP Global Forecast System (GFS) with the contribution of dropwindsonde data when Sinlaku was located southeast of Taiwan. This paper aims to examine how these targeted dropwindsonde data lead to track forecast improvements.

Tropical cyclone motion is mainly controlled by the environmental steering flow (e.g., Chan and Gray 1982). Therefore, analysis of the steering flow associated with the various systems can be useful to understand the factors contributing to track forecast improvements. Potential vorticity (PV) diagnosis has been applied to investigate the influence of the large-scale environmental flow and the different synoptic features on TC tracks in a number of publications (e.g., Wu and Emanuel 1995a,b; Shapiro 1996, 1999; Wu and Kurihara 1996; Wu and Wang 2000, 2001; Wu et al. 2004). In particular, the steering-flow effects associated with the binary interaction and a midlatitude trough have been quantitatively assessed and explored based on the PV diagnosis (Wu et al. 2003, 2009b; Yang et al. 2008). To better understand the key factors affecting the track of Sinlaku and to evaluate how the additional data improve track forecasts, detailed PV diagnosis of how synoptic features in the model are impacted by the assimilation of dropwindsonde data is reported. The description of the data and PV analyses is presented in section 2. A synopsis of Typhoon Sinlaku and PV diagnosis of its motion are shown in section 3. The data impact and the steering flow identified using PV inversion in model runs with and without dropwindsondes are presented in section 4. Finally, section 5 presents the summary.

2. Data and analysis method

a. Data

1) NCEP GTA GLOBAL ANALYSES

This study utilizes the Global Tropospheric Analyses (GTA) from the Final Global Data Assimilation System

(GDAS FNL) of NCEP to conduct PV diagnosis as described in section 2b. The horizontal resolution of the grid data is 1° × 1° (longitude by latitude) analyzed 4 times each day, with the 26 layers in the vertical from 1000 to 10 hPa.

2) NCEP GFS GLOBAL FORECASTS

In addition to using GTA analyses to understand key factors affecting the motion of Typhoon Sinlaku, the PV diagnosis based on model output data of NCEP GFS is also performed to evaluate the impact of dropwindsonde data on numerical forecasts. The model run in which the dropwindsonde data were assimilated into the NCEP model is denoted as GFS-WD, and that without any dropwindsonde data assimilated (i.e., denial run) is denoted as GFS-ND. The case examined here is initialized at 0000 UTC 10 September 2008 for Typhoon Sinlaku. During this period, dropwindsonde data were collected from the DOTSTAR Astra; the dropwindsonde data near the TC core acquired by WC-130J are excluded from the NCEP GFS data assimilation system (Aberson 2003, 2008). It should be stressed that the only difference between the two parallel runs lies in the use of dropwindsonde data in the assimilation system.

For GFS-WD, the dropwindsonde data are assimilated in the update cycle in the NCEP model. Thus, the background field (the first guess) contains information from previous dropwindsonde data. For GFS-ND, dropwindsonde data are removed globally. The model run is initialized when the first dropwindsonde data are assimilated into the model for a particular TC or set of TCs and continues until 12 h after the last mission is completed (Aberson and Etherton 2006; Aberson 2011; Chou et al. 2011), in this case beginning 0000 UTC 27 August and ending 1200 UTC 2 October 2008. Accordingly, two analyses of this case are produced using different first-guess fields. The impact of assimilating dropwindsondes from previous analysis times is discussed in section 4a.

The NCEP GFS (Han and Pan 2011) is an operational global data assimilation and model system providing forecasts four times per day. During 2008, the horizontal resolution was spectral triangular 382 (T382). The vertical coordinate extends from the surface to about 2.7 hPa with 64 unequally spaced sigma levels on a Lorenz grid. The GDAS is composed of a quality control algorithm, a vortex relocation procedure, an analysis procedure, and the NCEP GFS itself (Aberson 2003). The NCEP GFS does not use any synthetic data for TC initialization, except when the vortex is too weak in the first-guess field. For the case studied in this paper, no synthetic data are applied.

b. PV diagnosis

A brief description of PV diagnosis is provided here; detailed methodology including piecewise PV inversion, the definition of the deep-layer-mean (DLM) steering flow, and the normalized steering effect associated with each PV perturbation in the along-track (AT) direction has been described in Wu et al. (2003, 2004) and Yang et al. (2008).

A consequence of PV invertibility is that, given a distribution of PV and prescribed balance and boundary conditions, the balanced mass and wind fields can be recovered. The special advantage of PV inversion comes from the so-called piecewise PV inversion, when the flow field is divided into the mean and perturbation components obtaining the balance fields associated with each individual PV perturbation (Davis 1992). Such a method can describe how different PV features and environmental perturbations affect the TC track.

To understand how the environmental flow affects TC motion, the average axisymmetric quantities relative to the storm center are defined as the mean, and the rest as the perturbation field. Then, the approach of Wu et al. (2003, 2004) is followed to perform piecewise PV inversion. The azimuthal average of the wind field is first calculated to obtain the mean streamfunction ($\overline{\Psi}$), so that the associated mean geopotential height ($\hat{\Phi}$) and PV ($\hat{q}$) fields can be derived from the nonlinear balance equation (Charney 1955) and the Ertel PV equation on π $[\pi = C_p(p/p_0)^\kappa]$ and spherical coordinates, respectively. By taking the perturbation field as $\Psi' = \Psi - \overline{\Psi}$, $\Phi' = \Phi - \hat{\Phi}$, and $q' = q - \hat{q}$, the piecewise PV inversion is performed to calculate the balanced flow and mass fields associated with each PV perturbation.

In the Sinlaku case, four common synoptic features in the western North Pacific are identified, and the total PV perturbation is divided into four PV perturbations based on the algorithm in Yang and Wu (2010): the Pacific subtropical high (q'_{SH}), the monsoon trough (q'_{MT}), the continental high (q'_{CH}), and the midlatitude trough (q'_{TR}). For the purpose of partitioning the PV, the boundary between the subtropical high and the continental high with negative PV perturbation is generally set along a line extending from 23°N, 120°E to 55°N, 160°E (just south of the Kamchatka Peninsula). The division between the midlatitude trough and the monsoon trough with positive PV perturbation usually falls between 23° and 25°N depending on their respective locations. The selection of PV perturbations corresponding to these synoptic features is subjective. In general, the boundary line that divides those perturbations is based on the location and size of these synoptic systems (see Fig. 4a for an outline of the four inverted PV regions).

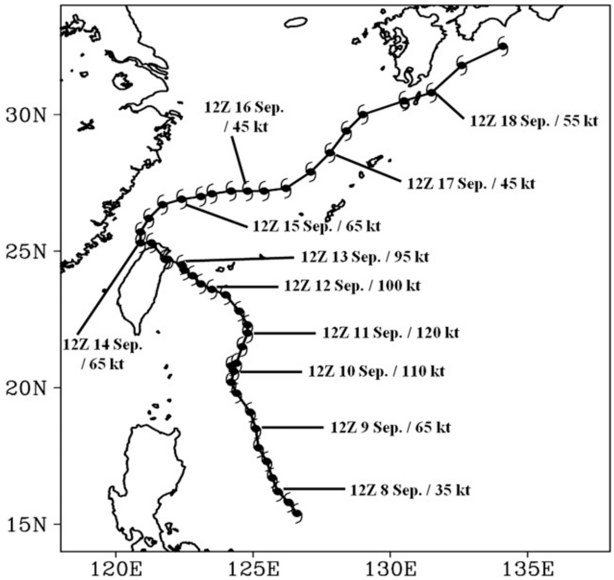

FIG. 1. JTWC best track of Typhoon Sinlaku from 0000 UTC 8 Sep to 0000 UTC 19 Sep 2008 for every 6 h. The number after the symbol "/" indicates the maximum wind (kt) analyzed by JTWC.

Following Wu et al. (2003) and Yang et al. (2008), the steering flow ($\mathbf{V}_{\mathrm{SDLM}}$) is defined as the 925–300-hPa wind vector averaged over the inner 3° latitude around the TC center (based on the location of the maximum 850-hPa PV). A sensitivity test in which the partition boundary is moved about 1° or 2° (longitude/latitude) has been conducted to examine the effects on the DLM (925–300 hPa) steering flow associated with each PV perturbation. For the NCEP global data with 1° resolution used in this study, the variation in the magnitude of the DLM steering flow ranges between approximately 2% and 4%, while the difference in the direction of the steering flow is within 10° (not shown). The DLM steering flow derived from the PV inversion is not sensitive to small-scale features (since PV inversion is a smoothing process; see Hoskins et al. 1985) at the edge of the PV perturbations. In addition, the value "AT" has been designed to quantitatively measure the influence of the steering flow associated with each PV perturbation in the direction parallel to the steering flow associated with the total PV perturbation (q'). Namely, AT for a particular PV perturbation (q'_s) is defined as

$$\mathrm{AT}(q'_s) \equiv \frac{\mathbf{V}_{\mathrm{SDLM}}(q'_s)\cdot\mathbf{V}_{\mathrm{SDLM}}(q')}{|\mathbf{V}_{\mathrm{SDLM}}(q')|^2}, \qquad (1)$$

where $\mathbf{V}_{\mathrm{SDLM}}(q'_s)$ and $\mathbf{V}_{\mathrm{SDLM}}(q')$ indicate the DLM steering flow associated with q'_s and q', respectively. The AT is a normalized quantity and, by definition, $\mathrm{AT}(q') = \mathrm{AT}(q'_s) + \mathrm{AT}(q'_{\mathrm{nos}})$, where q'_{nos} represents the rest of the PV perturbation other than q'_s, and $q' = q'_s + q'_{\mathrm{nos}}$.

3. GTA analyses

a. Synopsis of Typhoon Sinlaku (2008)

The best track and the intensity of Typhoon Sinlaku analyzed by the Joint Typhoon Warning Center (JTWC) are shown in Fig. 1. Sinlaku was formed at 1800 UTC 8 September east of the Philippines. It moved very slowly northward with a translation speed of around 1.9 m s^{-1} and reached its maximum intensity of 125 kt (1 kt = 0.5144 m s^{-1}) at 1800 UTC 10 September. For the runs initialized at 0000 UTC 10 September, GFS-ND shows a larger eastward track bias than GFS-WD after 36 h (see Fig. 7). On 12 September, Sinlaku gradually turned to the northwest toward Taiwan and made landfall near the northeastern tip of the island about two days later. After passing through northern Taiwan, Sinlaku recurved northeastward before undergoing an extratropical transition to the south of Japan.

The 850-hPa streamlines and the 500-hPa geopotential height and wind speed from the NCEP GTA analyses are shown in Figs. 2 and 3, respectively. The streamlines at 0000 UTC 10 September (Fig. 2a) show that the cyclonic circulation within about 3000 km accompanying Sinlaku (indicated by the dashed contour in Fig. 2a) is generally larger than that of a typical TC, indicating that Sinlaku was embedded within a monsoon trough. The monsoon trough axis extends from the east-northeast to the west-southwest (Figs. 2b,c), similar to the reverse-oriented pattern over the western North Pacific addressed in Lander (1996). The reverse-oriented pattern remains until 0000 UTC 12 September (Figs. 2d,e), and then an anticyclonic circulation gradually builds and extends to the northeast and northwest of Sinlaku (Fig. 2f). The change in the motion toward the northwest (Fig. 1) is attributed to the variation of the environmental flow around Sinlaku.

The Pacific subtropical high weakens with time (Figs. 3a–c) and recedes to the east of 145°E at 1200 UTC 11 September (Fig. 3d; indicated by the 5880-gpm contour), leading to the northward motion of Sinlaku. Afterward, the subtropical high expands westward near 130°E on 12 September (Figs. 3e,f), pushing Sinlaku to turn to the northwest. Meanwhile, the continental high strengthens (Figs. 3a,b) and weakens afterward (Figs. 3c–f). The subtlety of the steering-flow change associated with the synoptic systems suggests that more observational data over the ocean around Sinlaku are required to better conduct precise analyses and thus to improve numerical model forecasts.

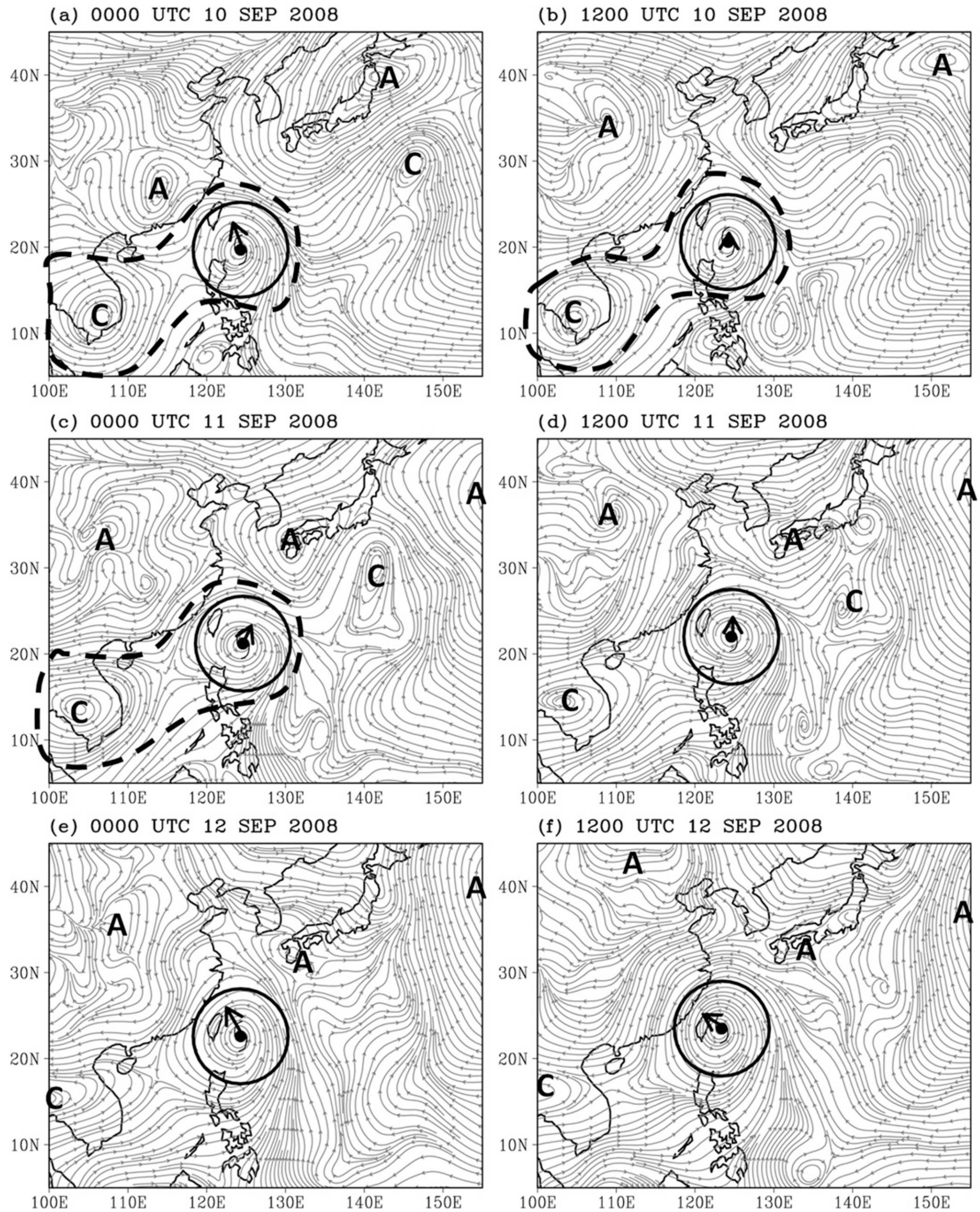

FIG. 2. Streamlines at 850 hPa from the NCEP GTA analyses starting from (a) 0000 UTC 10 Sep to (f) 1200 UTC 12 Sep 2008 at 12-h intervals. The instantaneous motion of Sinlaku is indicated by the thick black arrow, the length of which represents the actual translation speed, and the circle shows the scale of 5 m s^{-1}. The letters ''C'' and ''A'' highlight the cyclonic and anticyclonic circulations, respectively. The area surrounded by the dashed contour in (a)–(c) indicates circulation related to the monsoon.

b. PV diagnosis of the motion of Sinlaku

The PV diagnosis based on the NCEP GTA analysis is explored. The total PV perturbation and the 925–300-hPa wind at different analysis times are shown in Fig. 4. There is no PV signal from Sinlaku in the PV perturbation field since the mean PV associated with Sinlaku has been removed. Figure 4 shows that a large area of positive PV perturbation to the southwest of Sinlaku is associated with the tropical monsoon trough

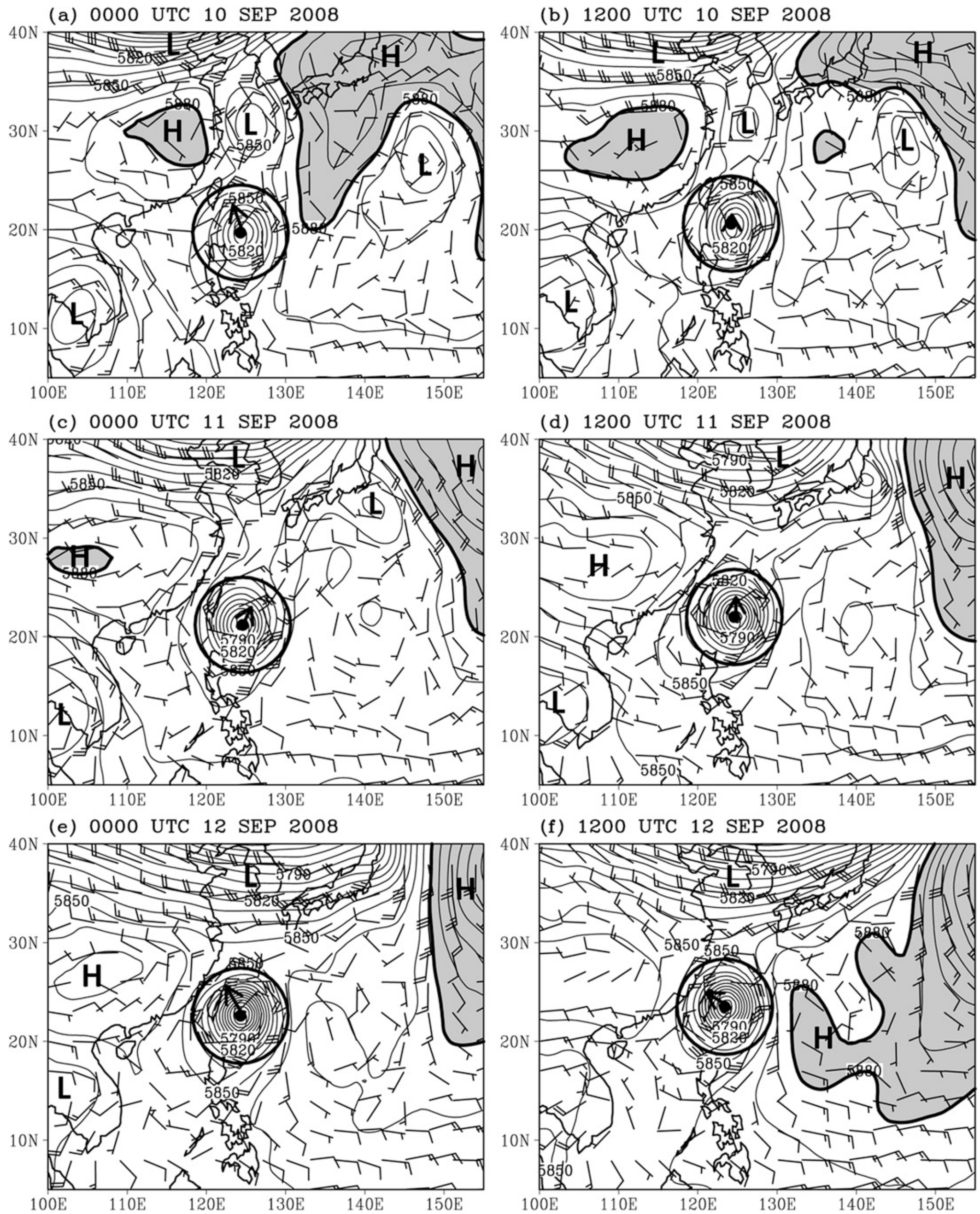

FIG. 3. Geopotential height (contour interval of 10 gpm; the area with values larger than 5880 gpm is shaded) and wind (one full wind barb = 5 m s^{-1}) at 500 hPa from NCEP GTA analyses starting from (a) 0000 UTC 10 Sep to (f) 1200 UTC 12 Sep 2008 at 12-h intervals. The letters ''L'' and ''H'' roughly indicate the low and the high systems, respectively. The definitions of the arrow and circle are as in Fig. 2.

(indicated by the dashed contour in Fig. 2). In addition, positive and negative PV perturbations are found to the north and east of Sinlaku. It is clear that the distribution of total PV perturbation in Fig. 4 is generally consistent with the synoptic features shown in Figs. 2 and 3. The criteria mentioned in section 2b are employed to divide the total PV perturbation into four pieces corresponding to the subtropical high, the monsoon trough, the continental high, and the midlatitude trough (i.e., $q' = q'_{SH} + q'_{MT} + q'_{CH} + q'_{TR}$; Fig. 4a).

Figure 5 is a time series of the 925–300-hPa steering flow ($\mathbf{V}_{SDLM}$) associated with each PV perturbation, the

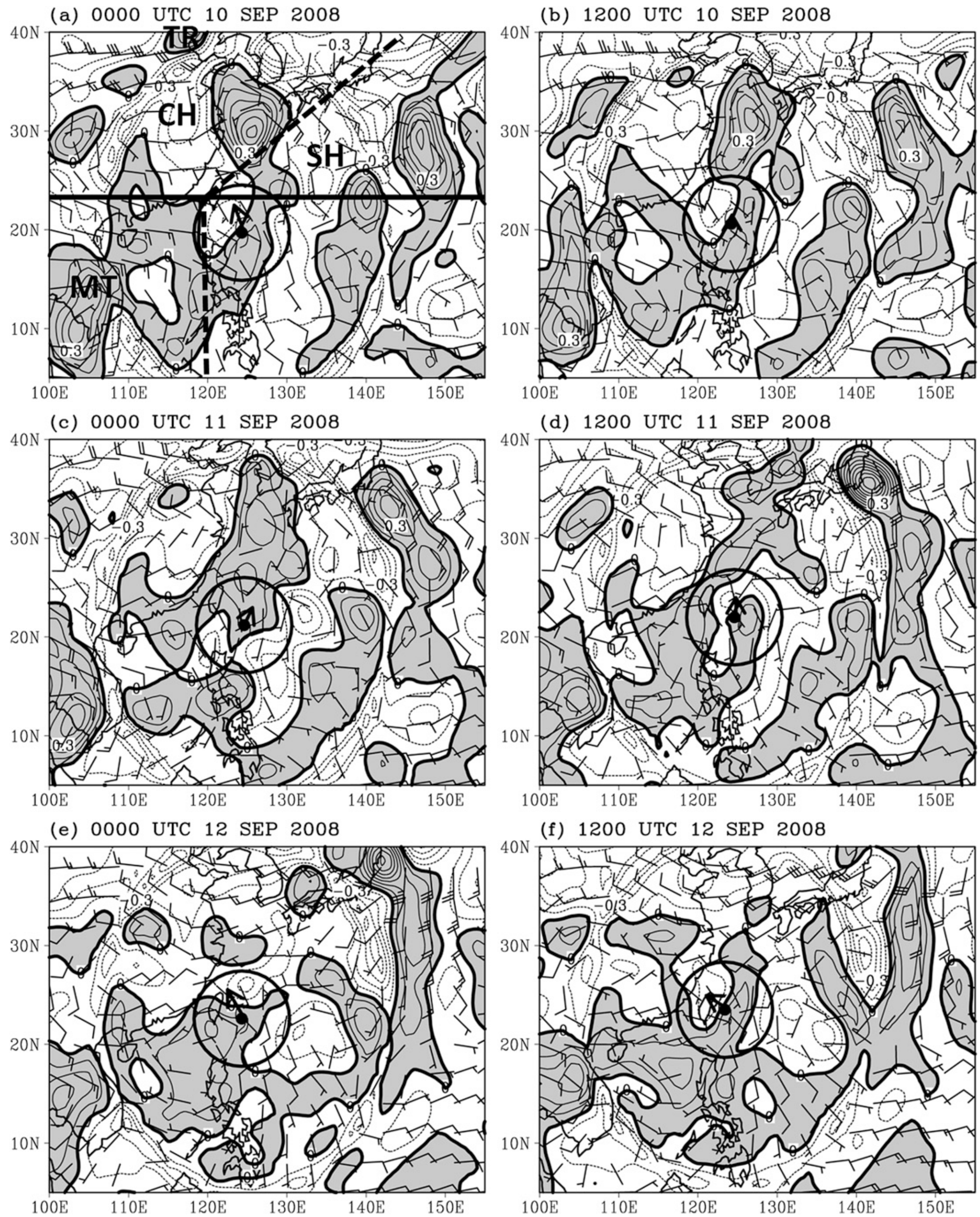

FIG. 4. Total potential vorticity perturbation [q'; scaled in 10^{-2} potential vorticity units (PVU), where 1 PVU = 10^{-6} K m^2 kg^{-1} s^{-1}; the positive PV perturbation is shaded with contour intervals of 0.1 PVU] at 500 hPa and the 925–300-hPa deep-layer-mean wind (one full wind barb = 5 m s^{-1}) from the NCEP GTA analyses starting from (a) 0000 UTC 10 Sep to (f) 1200 UTC 12 Sep 2008 at 12-h intervals. The definitions of the arrow and circle are the same as in Fig. 2. The solid (dashed) line in (a) generally indicates the partition boundary of the positive (negative) PV perturbation between the trough and the monsoon trough (between the subtropical high and the continental high).

model TC motion in the NCEP GTA ($\mathbf{V}_{AF}$), and the analyzed best track motion [estimated from the 12-h positions ($\mathbf{X}$), i.e., $\mathbf{V}_{BT} = (\mathbf{X}_{t+6h} - \mathbf{X}_{t-6h})/12\,h$]. A comparison of wind barbs in the bottom three rows in Fig. 5 shows that the magnitude of the balanced flow associated with all PV perturbations combined [$\mathbf{V}_{SDLM}(q')$] is roughly a factor of 2 larger than the actual TC speed ($\mathbf{V}_{BT}$ and/or $\mathbf{V}_{AF}$) at nearly every analysis time, although their directions are generally consistent. To examine the appropriateness of using the DLM wind associated with PV

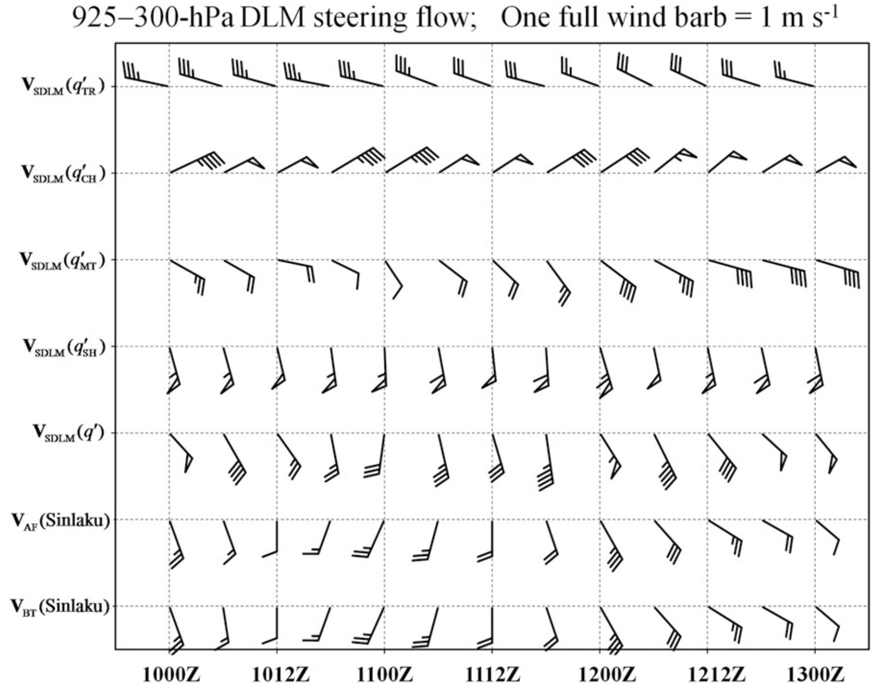

FIG. 5. Time series of the best track of Sinlaku [$\mathbf{V}_{\mathrm{BT}}$ (Sinlaku)], with its motion analyzed in NCEP GTA data [$\mathbf{V}_{\mathrm{AF}}$ (Sinlaku)]. The steering flow is associated with the total PV perturbation [$\mathbf{V}_{\mathrm{SDLM}}(q')$], the subtropical high [$\mathbf{V}_{\mathrm{SDLM}}(q'_{\mathrm{SH}})$], the monsoon trough [$\mathbf{V}_{\mathrm{SDLM}}(q'_{\mathrm{MT}})$], the continental high [$\mathbf{V}_{\mathrm{SDLM}}(q'_{\mathrm{CH}})$], and the midlatitude trough [$\mathbf{V}_{\mathrm{SDLM}}(q'_{\mathrm{TR}})$] from 0000 UTC 10 Sep to 0000 UTC 13 Sep 2008 at 6-h intervals. One full wind barb (flag) represents 1 (5) m s^{-1}.

features, the TC motion and the steering associated with the total PV perturbation within the deep (e.g., 925–300, 850–300, and 700–300 hPa) and mid- to lower (e.g., 925–500, 850–500, and 700–500 hPa) troposphere are compared. The balanced steering flow, whether in the deep layer or in the mid- to lower troposphere, is still faster than the TC translation speed at nearly every analysis time (not shown). It is not clear why the actual TC translation speed is not consistent with the balanced steering flow based on the PV diagnosis. The PV diagnosis has limitations in accurately identifying the actual TC speed for this particularly slow-moving (~7 km h^{-1}) case. Previous studies based on the same technique (e.g., Wu et al. 2003, 2004; Yang et al. 2008) have demonstrated that the PV analysis characterizes the TC motion when the storm translation speed is faster than in this case. The comparison between $\mathbf{V}_{\mathrm{SDLM}}(q'_{\mathrm{SH}})$ and $\mathbf{V}_{\mathrm{SDLM}}(q')$ indicates that the northward motion of Sinlaku is primarily attributed to the Pacific subtropical high. The DLM steering flow associated with the monsoon trough [$\mathbf{V}_{\mathrm{SDLM}}(q'_{\mathrm{MT}})$] ranges between 2.0 and 2.5 m s^{-1} before 1200 UTC 10 September, when it is reduced to near 1.0 m s^{-1} until 0000 UTC 11 September. Afterward the steering flow becomes larger and remains around 4.0 m s^{-1} after 0000 UTC 12 September, which is almost twice the speed of the steering flow on 10 September. It is indicated that the monsoon trough plays an important role in steering Sinlaku at later times. In contrast, the DLM steering flow associated with the continental high [$\mathbf{V}_{\mathrm{SDLM}}(q'_{\mathrm{CH}})$] moves southwestward steadily at 4.0–5.5 m s^{-1}, and the midlatitude trough [$\mathbf{V}_{\mathrm{SDLM}}(q'_{\mathrm{TR}})$] contributes between 2.5 and 3.5 m s^{-1} toward the southeast, contrary to the northwestward motion of Sinlaku. Overall, the DLM steering flow around Sinlaku is affected mainly by the Pacific subtropical high at the average speed of 5.6 m s^{-1}, and second by the continental high at 4.7 m s^{-1}. The comparison between $\mathbf{V}_{\mathrm{BT}}$ and the steering flow associated with the individual PV perturbation also suggests that the steering direction associated with the Pacific subtropical high is generally consistent with the actual motion of Sinlaku.

Figure 6 shows the time evolution of AT as defined in section 2b associated with the four PV perturbations, or the projections of the steering flows parallel to the entire steering-flow vector defined as the balanced flow associated with the combination of all PV perturbations.[1] It

[1] Note that this is different than the best track motion vector previously used in Wu et al. (2003).

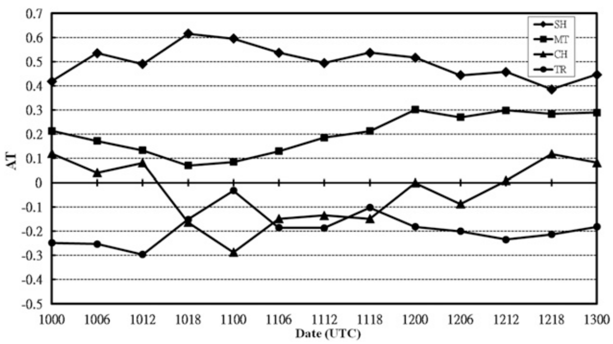

FIG. 6. Time series of AT for the PV perturbation associated with the subtropical high (diamond), the monsoon trough (square), the continental high (triangle), and the midlatitude trough (circle) from 0000 UTC 10 Sep to 0000 UTC 13 Sep 2008.

should be noted that the cross-track effect cannot be identified by the design of AT. It is obvious in Fig. 6 that the AT associated with the Pacific subtropical high (q'_{SH}) is always larger than 0.4 from 0000 UTC 10 to 13 September except at 1800 UTC 12 September, which indicates its major and continuous contribution to the along-track steering flow of Sinlaku. The AT associated with the continental high (q'_{CH}) shows positive values before and after 1200 UTC 10 and 12 September, but negative values during the intervening time, indicating an opposite steering effect to the northward motion of Sinlaku. Concerning the contribution from the two high pressure systems, the AT (values with two opposite signs mean the steering effect is canceled out) ranges from 0.31 to 0.58 with an average of 0.46. In other words, the DLM steering flow associated with the two high pressure systems would account for 46% of the steering flow associated with all PV perturbations combined. The remaining steering-flow contribution is expected to come from other features, as well as the uncertainty (about 10%; Wu and Emanuel 1995a,b) associated with the PV inversion.

The AT associated with the monsoon trough (q'_{MT}) drops to 0.07 at 1800 UTC 10 September before gradually rising and finally remaining around 0.3 after 0000 UTC 12 September. Indeed, the monsoon trough plays a secondary role in contributing to the along-track component of the steering with the positive AT values during the 3-day period. On the contrary, the AT associated with the midlatitude trough (q'_{TR}) is always negative, indicating a steering-flow direction against the motion of Sinlaku.

In summary, the averages of absolute AT values associated with the subtropical high, monsoon trough, continental high, and midlatitude trough from 0000 UTC 10 to 13 September are about 0.50, 0.20, 0.11, and 0.19, respectively (Fig. 6), though the latter two are in the opposite direction of the overall balanced steering flow. Based on the definition of AT, these values represent the relative contribution to the overall balanced steering flow. Therefore, it can be concluded that the Pacific subtropical high has primary influence (i.e., 50%) on the steering flow of Sinlaku, and the influences of the monsoon trough and midlatitude trough are secondary, with about 20% contribution each. It is worth noting that the overall steering flow that advects the TC is a composite of these. The merit of AT lies in its ability to quantitatively identify relative contribution of individual components of the steering flow based on piecewise PV inversion, since the cross-track components of the steering flow should be cancelled out between PV perturbations. The large track forecast errors in the case of Sinlaku might be attributed to the variation in the strength and size of these synoptic features, highlighting the importance of accurately representing these features with improved model initial conditions employing advanced data assimilation systems. The impact of dropwindsonde data on the NCEP GFS analysis and model forecasts and the roles of these synoptic features in providing the steering flow based on the PV diagnosis are further explored in the next section.

4. GFS forecasts

a. Impact of dropwindsonde data

Figure 7 shows the best track and simulated tracks initialized at 0000 UTC 10 September (figure adapted from Chou et al. 2011). The GFS-ND track has a large eastward bias toward Japan after 48 h, whereas the GFS-WD track more accurately moves northwestward and makes landfall on Taiwan around 96 h. The track error is reduced from 377 km in GFS-ND to 68 km in GFS-WD at 72 h. The assimilation of dropwindsonde data leads to an improvement in the 12–96-h mean track forecast of up to 76%. The track forecasts within the first 36 h are degraded with the dropwindsonde data assimilated, but both forecasts are very good and the differences are very small.

The initial 500-hPa geopotential height, PV, and wind fields and their differences are shown in Figs. 8a–c. To avoid mask effect caused by the TC center displacement and to clearly show the environmental fields, the filtering method of Kurihara et al. (1993, 1995) is adopted here. The cyclonic circulation associated with the upper-level low to the north of Sinlaku is evident in both GFS-ND (Fig. 8a) and GFS-WD (Fig. 8b), but that in GFS-WD is weak, with a relatively low PV at its center. The Pacific subtropical high to the south of Japan in GFS-WD (Fig. 8b) extends slightly more southward to near 20°N (indicated by the contour of 5880 gpm) than that in GFS-ND (Fig. 8a). Moreover, the difference in the 500-hPa geopotential height (Fig. 8c) indicates that the subtropical

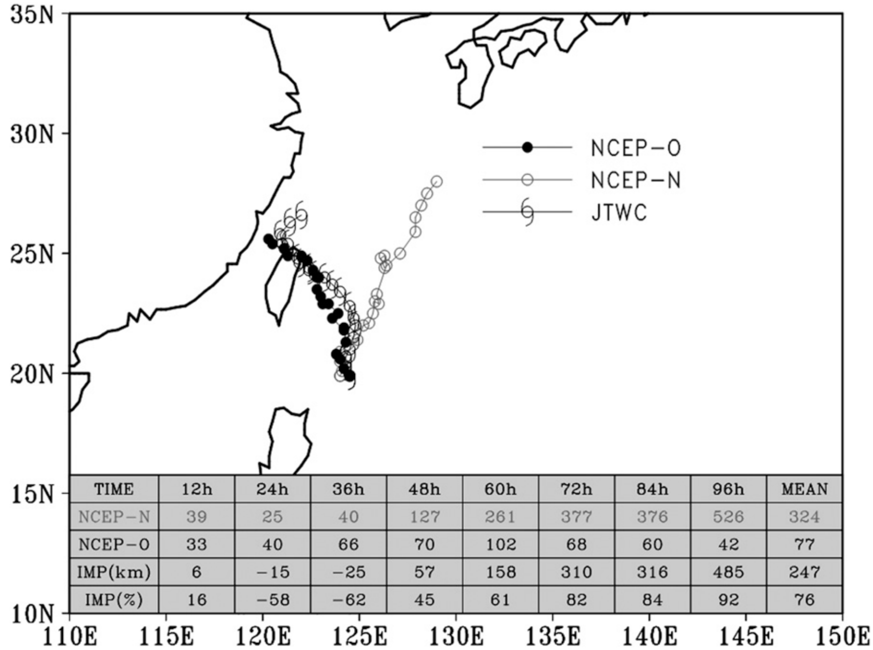

TIME	12h	24h	36h	48h	60h	72h	84h	96h	MEAN
NCEP−N	39	25	40	127	261	377	376	526	324
NCEP−O	33	40	66	70	102	68	60	42	77
IMP(km)	6	−15	−25	57	158	310	316	485	247
IMP(%)	16	−58	−62	45	61	82	84	92	76

FIG. 7. The JTWC best track (typhoon symbols) and the track forecasts of Sinlaku in GFS-ND (open circles) and GFS-WD (closed circles) for 120 h initialized at 0000 UTC 10 Sep 2008 (from Chou et al. 2011). Track errors (km) are shown at the bottom of the figure. NCEP-N (NCEP-O) is the track error in GFS-ND (GFS-WD). IMP (%) represents the track error improvement.

high to the east of Sinlaku becomes strengthened after the assimilation of the dropwindsonde data. Since the vortex associated with Sinlaku has been filtered out, the height rise to the northeast of the TC related to the strengthening of the subtropical high can be clearly identified. As mentioned in section 2a, the background field used in the update cycle in GFS-WD includes information from previous dropwindsonde data in addition to those at the analysis time. We have examined how dropwindsonde data at this and previous times produce the analysis increment. The forecast fields initialized at previous analysis times are taken as the first guess. The 12-h 500-hPa forecast fields from GFS-WD and GFS-ND runs initialized at 1200 UTC 9 September (i.e., valid at 0000 UTC 10 September) are shown. The difference of the 500-hPa geopotential height and wind between GFS-WD and GFS-ND (Fig. 8d) can be regarded as the difference in the first guess between the two runs that resulted from assimilating dropwindsonde data at previous times. Meanwhile, the analysis increment in Fig. 8c comes from the assimilation of dropwindsonde data at 0000 UTC 10 September, in addition to that at previous times. Some distinct differences in Fig. 8c, such as the feature near 150°E and the upper-level low to the south of Korea, are found to be well connected to the differences in the first guess (Fig. 8d). This indicates that the analysis increment results from the accumulated effect of previous dropwindsonde data and from the data assimilated at the analysis time. The direct impact of dropwindsonde data at this time may not be clearly identified since the first-guess field in GFS-WD contains information from the data of previous times. Figure 9 shows the 72-h 500-hPa geopotential height and wind field. The subtropical high to the northeast of Sinlaku in GFS-ND is weaker and smoother (Fig. 9a) than that in GFS-WD (Fig. 9b). The GFS-WD field appears to more resemble the GTA analyses (Fig. 9c). The presence of the subtropical ridge would likely cause the TC in GFS-WD to move northwestward, and thus its landfall over Taiwan is correctly predicted. In addition, the geopotential height associated with the midlatitude trough in GFS-ND appears deeper than that in GFS-WD.

The initial 925–300-hPa wind velocity and the difference between GFS-WD and GFS-ND are displayed in Figs. 10a–c. The asymmetric structure of the cyclonic circulation associated with Sinlaku is seen in both runs (Figs. 10a,b), with relatively high wind speeds on the eastern side. The TC in GFS-WD has a maximum DLM wind exceeding 21 m s^{-1} east of the center (Fig. 10b), whereas the area of maximum wind speed in GFS-ND is broader than in GFS-WD, but with a magnitude below 15 m s^{-1} (Fig. 10a). The circulation center in GFS-WD

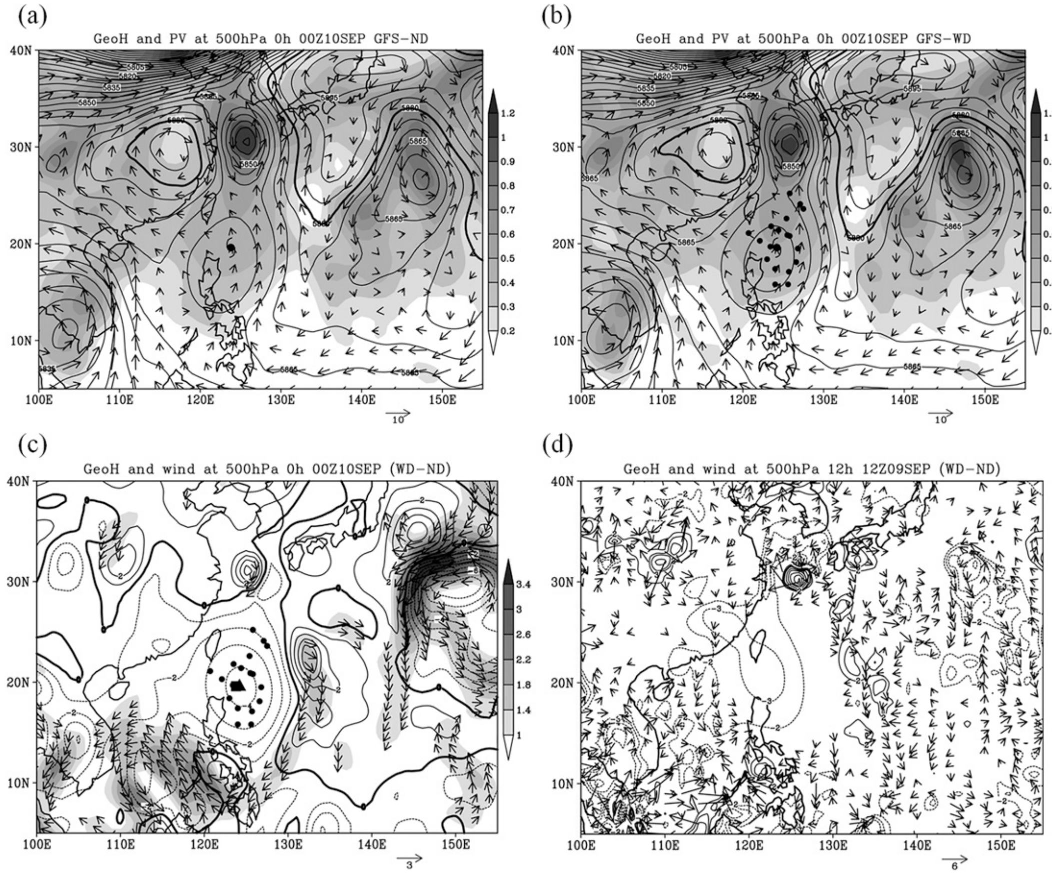

FIG. 8. Geopotential height (contour intervals of 5 gpm), PV (shading; PVU), and wind (vector; m s^{-1}) at 500 hPa at 0000 UTC 10 Sep 2008 in (a) GFS-ND and (b) GFS-WD with TC components filtered out. The difference of geopotential height (contour intervals of 1 gpm) and wind (vector; m s^{-1}) at 500 hPa between GFS-WD and GFS-ND with TC components filtered out at (c) 0 h initialized at 0000 UTC 10 Sep and (d) 12 h initialized at 1200 UTC 9 Sep 2008. In (c),(d), wind vectors with values smaller than 1 m s^{-1} are omitted. Dots indicate locations where dropwindsondes are deployed by DOTSTAR.

(Fig. 10b) is closer to that in the best track than that in GFS-ND (Fig. 10a). The circulation center in GFS-ND is nearly 100 km southwest of the GFS-WD position (indicated by the triangular mark in Fig. 10a). Although the vortex repositioning/relocation algorithm is used in the first-guess field of both runs before any data assimilation, the dropwindsonde data may move the vortex. In addition, there is high uncertainty in identifying the center since the cyclonic circulation in GFS-ND is relatively broad and weak. This center position bias might be another source of track forecast errors. The DLM wind difference (Fig. 10c) shows the cyclonic flow pattern. The anticyclonic wind difference between 128° and 133°E is due to the strengthened Pacific subtropical high in GFS-WD.

Figure 11 shows the initial azimuthal mean tangential wind speeds extending 10° outward at 1000, 850, and 500 hPa. It is noticeable that the maximum tangential wind speeds in GFS-WD at all three levels are larger than those in GFS-ND. Additionally, the 850-hPa radius of maximum wind speed in GFS-WD (Fig. 11) is approximately 250 km, whereas it is about 400 km in GFS-ND, indicating that the initial GFS-WD vortex is relatively compact and strong. This is consistent with Aberson (2011), who showed that the initial vortex is generally stronger in the NCEP GFS with dropwindsonde data assimilated than in the GFS without them. Nevertheless, due to the coarse resolution of the NCEP GFS, the vortex structure in GFS-WD is still far from the actual TC in the best track data. The radius of 34-kt wind speed taken from the JTWC best track data averages about 90 nm (167 km) at 0000 UTC 10 September. The maximum wind speed at 1000 hPa in GFS-WD is about 14 m s^{-1}, indicating that there is no 34-kt wind radius near the surface analyzed in the GFS model. Only a slight difference in the wind fields between the two runs (Fig. 11)

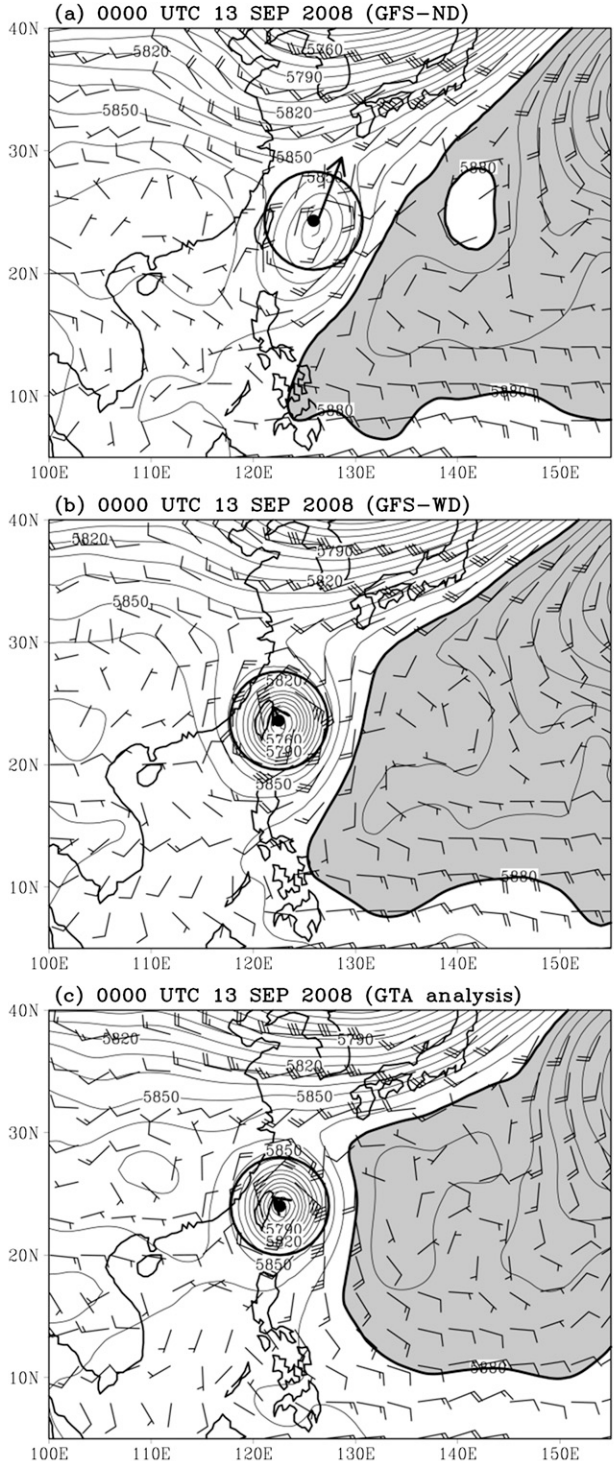

FIG. 9. As in Fig. 3, but valid at 0000 UTC 13 Sep 2008 in (a) GFS-ND, (b) GFS-WD, and (c) GTA analyses. In (a),(b), the initial time is 0000 UTC 10 Sep 2008.

about 500 km away from the TC center is seen since the outermost dropwindsonde data are located at that distance (Fig. 10b). Overall, Figs. 8–11 indicate that the assimilation of dropwindsonde data modifies the synoptic features in the vicinity of Sinlaku. Meanwhile, the assimilation would also help improve the initial GFS vortex structure in this case, although the improvement is still relatively small as compared to the TC structure indicated in the JTWC best track data.

To better understand the distinct differences between the tracks in Fig. 7, the 12-h mean TC motion is compared to the steering flow in these two runs at 0 and 48 h (Fig. 12a). The steering flow is defined as the azimuthal average wind velocity in a circle of 3° radius around the TC center. The steering-flow directions in both runs are generally consistent between various radii (from 3° to 7°), and the magnitudes have a maximum difference of about 1.0 (0.5) m s^{-1} in GFS-WD (GFS-ND; figure not shown). Thus, the impact of the radius on the steering-flow calculations is negligible. Both steering flows averaged between 925 and 300 hPa and between 925 and 500 hPa are shown (Fig. 12a), since it is found that they are closer to the TC motion than those from other vertical layers. In GFS-WD, the direction of the initial 925–300-hPa steering flow is consistent with the TC motion, although the magnitude is smaller. Both initial 925–300- and 925–500-hPa steering flows in GFS-ND point toward the northwest at about 1.5 m s^{-1}. The direction of the 925–500-hPa steering flow is closer to the TC motion than that of the 925–300-hPa steering flow although its direction is nearly 50° from that of the TC. At 48 h, the 925–300-hPa steering flow in GFS-WD generally agrees with the actual TC motion, whereas the 925–500-hPa steering flow is northward. In contrast, the 925–300-hPa steering flow in GFS-ND is quite different from the northeastward TC motion. The 925–500-hPa steering-flow direction is consistent with the TC motion. However, the 925–500-hPa steering flow of about 1 m s^{-1} is much weaker than the translation speed of nearly 3 m s^{-1}. Figure 12a indicates that the TC in GFS-WD is advected mainly under the influence of the 925–300-hPa steering flow, whereas the TC motion in GFS-ND appears closer to the 925–500-hPa mean flow. Figure 12b shows the time evolution of the steering-flow difference between 925–300-hPa wind in GFS-WD and 925–500-hPa wind in GFS-ND based on Fig. 12a. The difference in the zonal steering flow is always negative except at the final time. In addition, the zonal steering-flow difference after 36 h is larger than that at earlier times. The meridional component of the steering-flow difference is not significant.

The discrepancy between the GFS-WD and GFS-ND steering flows calculated through different vertical layers can be explained by the difference in the vertical structure

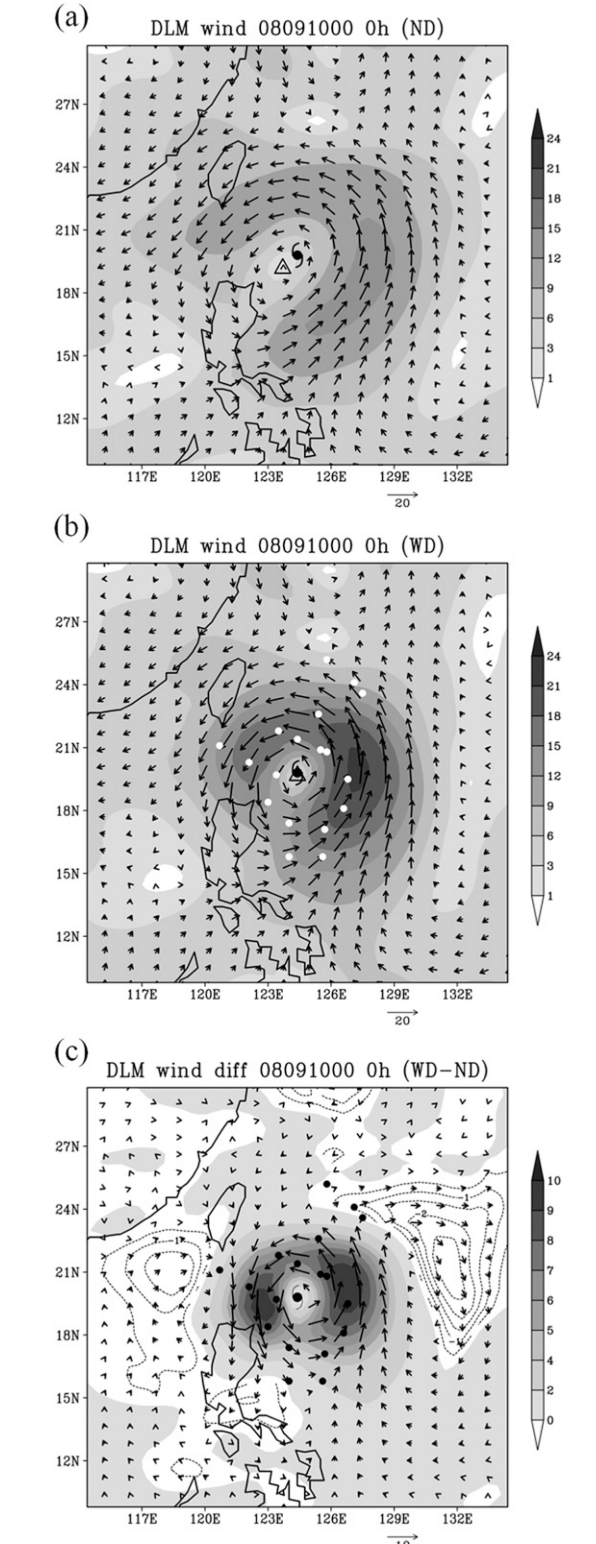

FIG. 10. The 925–300-hPa DLM wind (m s^{-1}) in (a) GFS-ND, (b) GFS-WD, and (c) the difference between GFS-WD and GFS-ND (positive: shading; negative: dashed contours with intervals of 0.5 m s^{-1}). The typhoon symbol and the triangle mark indicate the TC centers in the best track and the GFS, respectively. Dots indicate locations where dropwindsondes are deployed by DOTSTAR.

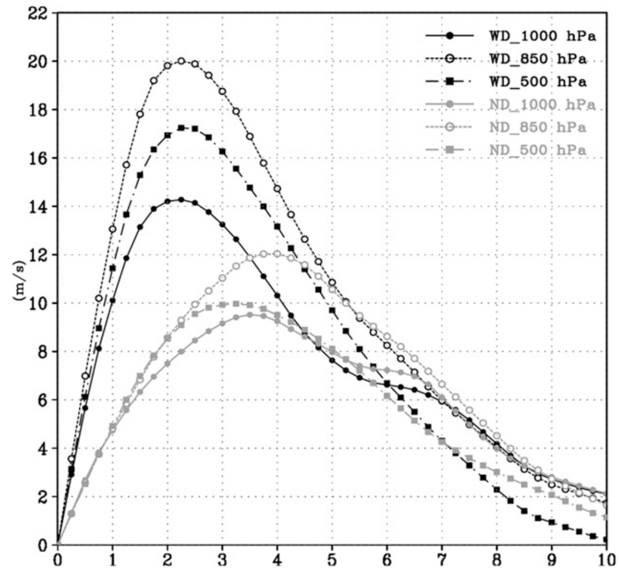

FIG. 11. The azimuthal mean of the tangential wind (m s^{-1}) extending 10° outward from the center of Sinlaku at 0000 UTC 10 Sep 2008 at 1000 (filled circle), 850 (open circle), and 500 (filled square) hPa in GFS-WD (black line) and GFS-ND (gray line).

in both runs (Fig. 13). Minor differences in the initial structure between the GTA analyses and GFS-WD (Figs. 13a,b) are due to the fact that the NCEP GTA analyses are prepared about an hour or so after the GFS is initialized. The initial vortex in GFS-WD extends higher in the troposphere and has larger tangential wind speeds (Fig. 13b) than that in GFS-ND (Fig. 13c). At later forecast times, the TC in GFS-WD intensifies slightly (Figs. 13e,h), so that it is similar to the analysis (Figs. 13d,g). In contrast, the vortex in GFS-ND persistently remains roughly between 1000 and 600 hPa with relatively weak tangential wind (Figs. 13f,i). Accordingly, the assimilation of dropwindsonde data improves the vertical structure at the initial time and throughout the forecast in the GFS. The relatively shallow vortex in GFS-ND would likely be controlled by the northeastward steering flow in the mid- to lower troposphere as indicated in Fig. 12a, thus leading to the track forecast bias. The improved vertical structure in GFS-WD would allow the TC to be advected predominantly by the 925–300-hPa steering flow that points toward the northwest (Fig. 12a). This is an important factor that gives rise to a more representative steering flow.

Another factor that can affect TC motion is the initial vortex size, which can lead to different rates of planetary vorticity advection. As suggested by DeMaria (1985), the vortex motion is much more sensitive to the vortex size than to the vortex intensity in a nondivergent barotropic model. In addition, Fiorino and Elsberry (1989) found that vortex motion induced by the planetary

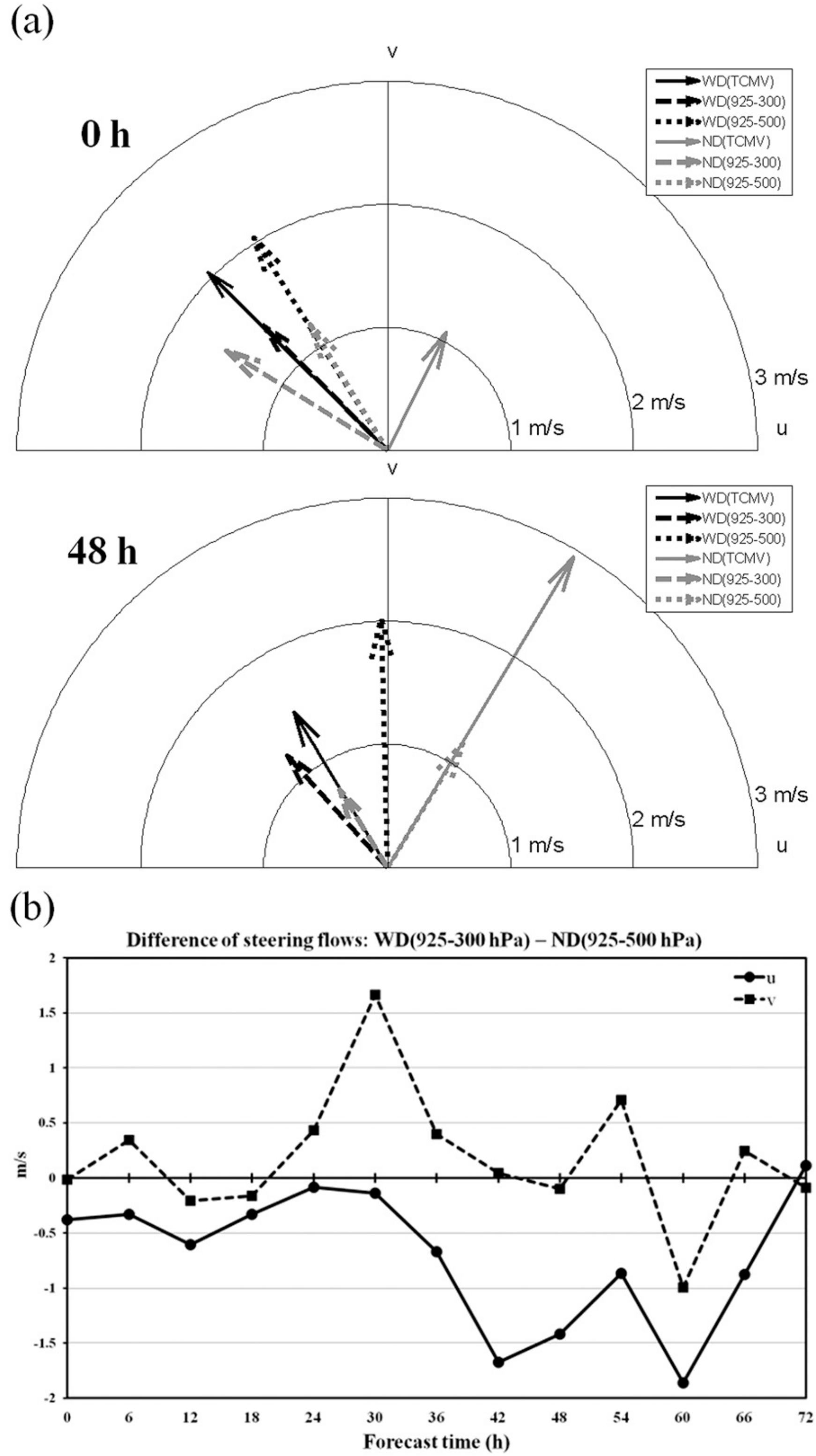

FIG. 12. (a) The 12-h mean TC motion in GFS-WD (solid black) and GFS-ND (solid gray), and the steering-flow vector between 925 and 300 hPa (dashed line) and that between 925 and 500 hPa (dotted line) in GFS-WD (black) and GFS-ND (gray) at (top) 0 and (bottom) 48 h initialized at 0000 UTC 10 Sep 2008. Each semicircle indicates a scale of 1 m s^{-1}. (b) The difference between the 925–300-hPa steering flow in GFS-WD and the 925–500-hPa steering flow in GFS-ND in zonal (solid line) and meridional (dashed line) components from 0 to 72 h initialized at 0000 UTC 10 Sep 2008.

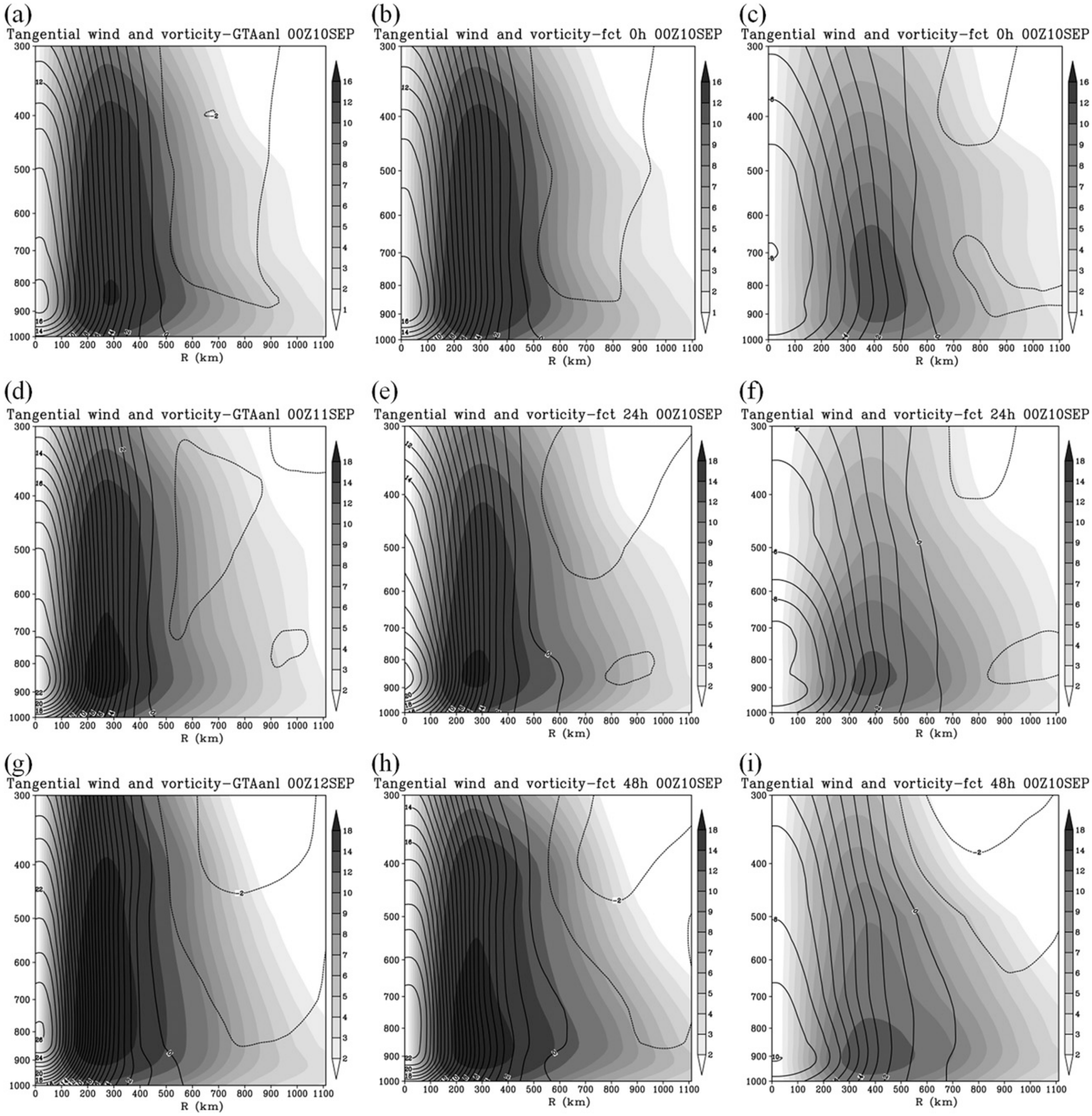

FIG. 13. The azimuthal mean structure of the tangential wind (shading; m s^{-1}) and the relative vorticity (contours with intervals of 1 $\times$ 10^{-5} s^{-1}) valid at 0000 UTC 10 Sep 2008 in (a) GTA analyses, (b) GFS-WD, and (c) GFS-ND. (d)–(f) As in (a)–(c), but valid at 0000 UTC 11 Sep 2008. (g)–(i) As in (a)–(c), but valid at 0000 UTC 12 Sep 2008. In GFS-WD and GFS-ND, the initial time is 0000 UTC 10 Sep 2008. The vertical pressure coordinate is in logarithmic scale.

vorticity advection by the vortex (i.e., the beta drift) highly depends on the flow 300–1000 km from the TC center. However, intensity changes in the inner region have little effect. The initial tangential wind profiles of GFS-WD and GFS-ND (Fig. 11) are not much different from each other beyond 5° from the center. Thus, the beta effect caused by the vortex size would likely have limited impact on the TC motion difference between the two runs.

b. PV diagnosis on forecasts with and without dropwindsonde data

Further analyses of PV diagnosis based on the GFS-WD and GFS-ND output have been conducted to connect

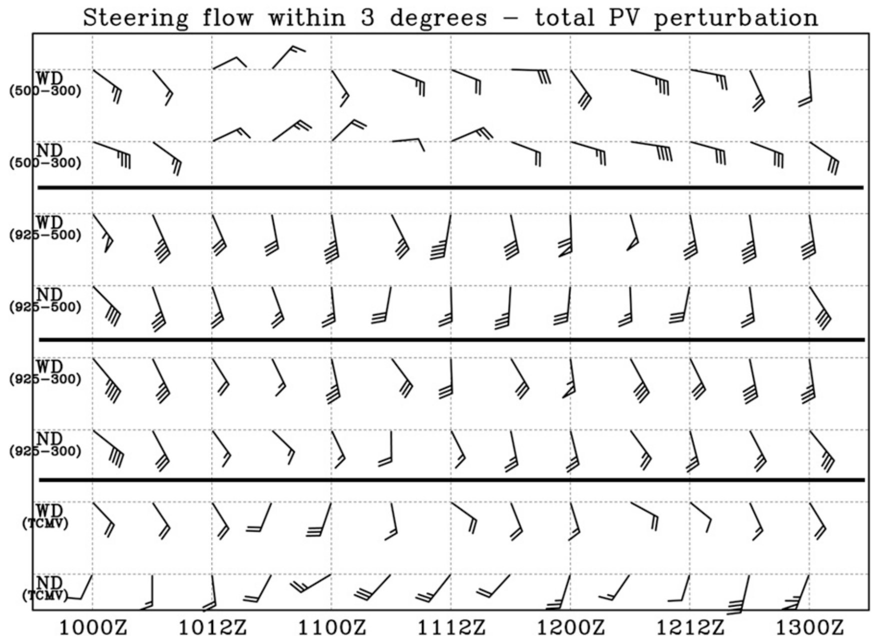

FIG. 14. Time series of the simulated TC motion (TCMV), and the steering flow associated with the total PV perturbation between 925 and 300 hPa, 925 and 500 hPa, 500 and 300 hPa in GFS-WD and GFS-ND (indicated by the row with "WD" and "ND", respectively) from 0000 UTC 10 Sep to 0000 UTC 13 Sep 2008 at 6-h intervals. One full wind barb (flag) represents 1 (5) m s^{-1}.

the PV analysis and the impact of the dropwindsonde data, and also to better understand how the track forecast is improved by the dropwindsonde data. Figure 14 shows the model TC motion and the steering flow associated with the total PV perturbation within three tropospheric depths (i.e., 925–300, 925–500, and 500–300 hPa) in GFS-WD and GFS-ND 3 days into the forecast. The (north) northwestward motion of the model TC in GFS-WD after 0000 UTC 11 September is generally consistent with the 925–300-hPa steering flow, though the translation speed is moderately slower than the flow. The steering flow in the upper troposphere between 500 and 300 hPa mostly points to the west in both runs. In GFS-ND, the 925–500-hPa steering flow tends to have a slightly larger eastward component than the 925–300-hPa steering flow, but it is not quite close to the northeastward motion of the model TC. It is not clear why there are large differences between the TC motion and PV-based steering flow. The PV diagnosis in this case study, unlike in previous studies (Wu et al. 2003, 2004; Yang et al. 2008), has its limitations and cannot accurately discern the TC motion. Nevertheless, the characteristics of inverted balanced steering flow in different layers are still qualitatively informative although quantitatively not representative of the steering flow derived from the azimuthal average (Fig. 12a).

To further examine which synoptic features identified in Fig. 4a are impacted by data assimilation, the balanced steering flow associated with each PV perturbation has been calculated based on the PV inversion. Based on Figs. 12 and 14, the presumption that the vortices in GFS-WD and GFS-ND are advected by the steering flows of different vertical layers appears to hold. Therefore, the steering flows between 925–300 hPa in GFS-WD and 925–500 hPa in GFS-ND are compared (Fig. 15). The difference in the model TC motion between GFS-WD and GFS-ND (the lowest row of wind barbs in Fig. 15) can be generally identified by the steering difference associated with the total PV perturbation (the second lowest row of wind barbs in Fig. 15) after 0000 UTC 11 September. However, the agreement between these two wind barbs is not good at all forecast times, likely due to the limitation of the PV inversion technique as mentioned earlier. The match of the two wind barbs appears reasonable for half of the times (e.g., 0000 UTC 11 September, 0600 UTC 11 September, 1800 UTC 11 September, 0600 UTC 12 September, and 1200 UTC 12 September) and is very different for the other half (e.g., 1200 UTC 11 September, 0000 UTC 12 September, 1800 UTC 12 September, and 0000 UTC 13 September). The steering-flow difference associated with the subtropical high and the monsoon trough mostly points to between the north and the west at the magnitude of about 0.5–2 m s^{-1} after 0000 UTC 11 September. The southeastward steering flow associated with the midlatitude trough in GFS-WD has a smaller eastward component than the GFS-ND (the first row of wind barbs in Fig. 15).

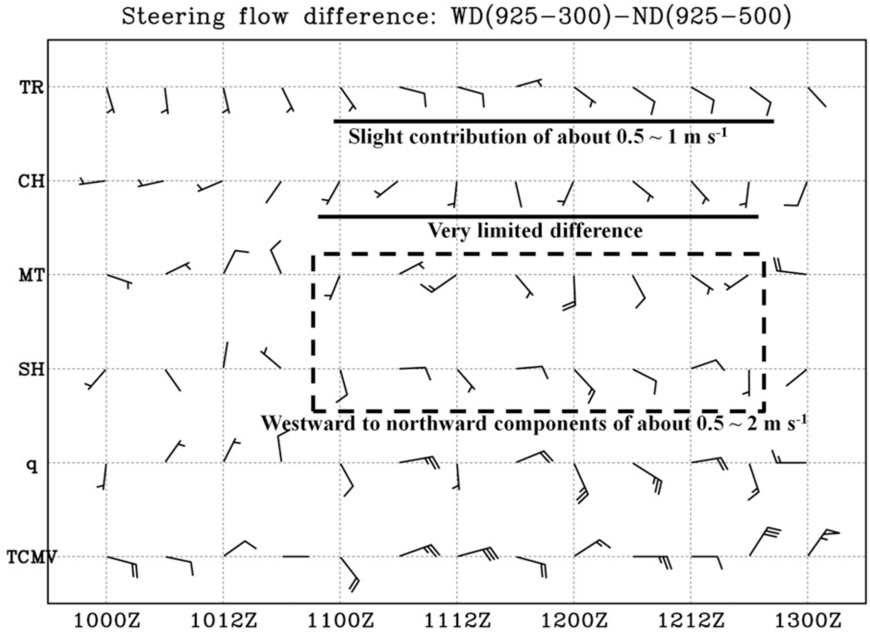

FIG. 15. Time series of the difference in the TC movement between GFS-WD and GFS-ND (TCMV), and the difference between the 925–300-hPa steering flow in GFS-WD and the 925–500-hPa steering flow in GFS-ND associated with the total PV perturbation (q), the subtropical high (SH), the monsoon trough (MT), the continental high (CH), and the midlatitude trough (TR) from 0000 UTC 10 Sep to 0000 UTC 13 Sep 2008 at 6-h intervals. One full wind barb (flag) represents 1 (5) m s^{-1}.

The steering-flow difference associated with the continental high is quite limited with the difference below 0.5 m s^{-1}. In all, Fig. 15 indicates that the model steering flow associated with the subtropical high and the monsoon trough is modified by the assimilation of dropwindsonde data contributing to the northwestward motion of Sinlaku, thus leading to improved track forecasts. Moreover, the influence of the midlatitude trough that impedes the TC motion also diminishes after the assimilation of the dropwindsonde data. The importance of better representation in the vertical vortex structure, and thus having reasonable steering flow in the deep troposphere based on the PV diagnosis during the forecast times, are highlighted. The PV diagnosis also identifies how the steering flow associated with each synoptic feature is impacted by the assimilation of the dropwindsonde data.

5. Summary

During the T-PARC field campaign in 2008, abundant dropwindsonde data were collected by both reconnaissance and surveillance flights throughout the lifetime of Typhoon Sinlaku. In particular, the track forecasts from the (ensemble) global models show large spreads and uncertainties when Sinlaku moved slowly to the southeast of Taiwan. In this study, the factors influencing the motion of Sinlaku with a very slow translation speed is investigated using PV diagnosis. Additionally, the two parallel runs (i.e., with and without the assimilation of dropwindsonde data, denoted as GFS-WD and GFS-ND, respectively) initialized at 0000 UTC 10 September 2008 are examined to assess the impact of those observations.

Based on PV diagnosis, the total PV perturbation is divided into four pieces, associated with the Pacific subtropical high, the monsoon trough, the continental high, and the midlatitude trough. The PV diagnosis shows that the DLM (925–300 hPa) steering flow around Sinlaku is primarily associated with the Pacific subtropical high with an average speed of 5.6 m s^{-1}. The quantitative evaluation of the steering flow in the along-track direction (AT) indicates that the subtropical high from 0000 UTC 10 to 13 September has an average of 50% contribution to the balanced steering flow associated with the total PV perturbation, while the influence from the monsoon trough becomes more significant with time. The complexity of the large-scale environmental flow in the vicinity of Sinlaku gives rise to the meandering motion. The poor skill in representing these synoptic features in the global models is one primary cause of large track forecast errors.

The assimilation of dropwindsonde data for the case initialized at 0000 UTC 10 September significantly reduces track forecast errors, with the 12–96-h mean improvement of up to 76% in the NCEP GFS (Chou et al. 2011). Due to the fact that two analyses are produced using different first guesses, the comparison between the analysis increment and the first guess indicates that the increment is caused by the accumulated effect of previous dropwindsonde data and by those assimilated at this analysis time. The initial 500-hPa subtropical high to the northeast of Sinlaku is stronger and larger in GFS-WD than that in GFS-ND, allowing the TC to move northwestward, consistent with the best track. The TC center in GFS-WD is closer to the best track position than that in GFS-ND. In addition to modifying the synoptic features, the structure and intensity of the initial vortex is improved with higher maximum tangential wind speeds and smaller radius of maximum wind speed in GFS-WD than in GFS-ND. The azimuthal average is carried out to remove the TC circulation and to obtain the steering flow across the TC. The TC motion in GFS-WD is consistent with the 925–300-hPa steering flow, whereas the TC motion in GFS-ND is mainly controlled by the steering flow between 925 and 500 hPa. This disagreement is attributed to the difference in the vertical vortex structure between these two runs. The shallow GFS-ND vortex appears to be influenced by the northeastward steering flow in the mid- to lower troposphere, thus leading to the track forecast bias. In all, the primary benefit from assimilating dropwindsonde data in this case is to improve the vertical vortex structure that extends farther into the troposphere. Therefore, the track forecast is improved with the storm vortex advected by a more representative steering flow in the deep troposphere.

To explore how model representation of the PV features associated with the synoptic systems would be impacted by assimilating dropwindsonde data, we have calculated the balanced steering flow based on PV diagnosis using GFS-WD and GFS-ND model outputs. The steering flows of different vertical extent in both GFS-WD and GFS-ND are qualitatively compared, and large differences between the TC motion and the PV-based steering flows are identified. The steering flow associated with the subtropical high and the monsoon trough is modified by assimilating dropwindsonde data to improve the northwestward motion of Sinlaku. In sum, the assimilation of dropwindsonde data allows the model to better represent the initial vortex structure, the center position, and the steering flow, thus improving the Sinlaku model forecasts.

Given the lack of a close match between the TC translation speed and the magnitude of the balanced PV-diagnosed steering flow, and the lack of a consistent relationship between TC motion and the PV-based steering flow, the utility of PV diagnosis appears limited in this case and might not accurately identify the motion of Sinlaku despite the success in applying the techniques in the past studies (Wu et al. 2003, 2004; Yang et al. 2008). The reasons why the capability of the PV inversion technique is constrained may include the slow TC speed (in the environment with weaker steering flow), but more needs to be investigated. Further examination of the impact on the evolution of TC intensity and structure and thus the representative steering flow is also needed to gain better insights into the overall value of dropwindsonde data and the basic TC dynamics.

Acknowledgments. The work is supported by the National Science Council of Taiwan through Grants NSC97-2111-M-002-016-MY3 and NSC98-2111-M-002-008-MY3, the Central Weather Bureau of Taiwan through Grants MOTC-CWB-97-6M-01 and MOTC-CWB-98-6M-01, and the Office of Naval Research Grant through N00173-08-1-G007 and N00014-10-1-0725. The authors are grateful to all collaborators contributing to the T-PARC project. The authors also thank Kun-Hsuan Chou and Yi-Shan Liao for their assistance in graphing. The valuable comments from two anonymous reviewers that helped improve the manuscript are also highly appreciated.

REFERENCES

Aberson, S. D., 2002: Two years of hurricane synoptic surveillance. *Wea. Forecasting,* **17,** 1101–1110.

——, 2003: Targeted observations to improve operational tropical cyclone track forecast guidance. *Mon. Wea. Rev.,* **131,** 1613–1628.

——, 2008: Large forecast degradations due to synoptic surveillance during the 2004 and 2005 hurricane seasons. *Mon. Wea. Rev.,* **136,** 3138–3150.

——, 2011: The impact of dropwindsonde data from the THORPEX–Pacific Area Regional Campaign and the NOAA Hurricane Field Program on tropical cyclone forecasts in the Global Forecasting System. *Mon. Wea. Rev.,* **139,** 2689–2703.

——, and J. L. Franklin, 1999: Impact on hurricane track and intensity forecast of GPS dropsonde observations from the first-season flights of the NOAA Gulfstream-IV jet aircraft. *Bull. Amer. Meteor. Soc.,* **80,** 421–427.

——, and B. J. Etherton, 2006: Targeting and data assimilation studies during Hurricane Humberto (2001). *J. Atmos. Sci.,* **63,** 175–186.

——, S. J. Majumdar, C. A. Reynolds, and B. J. Etherton, 2011: An observing system experiment for tropical cyclone targeting techniques using the Global Forecast System. *Mon. Wea. Rev.,* **139,** 895–907.

Chan, J. C.-L., and W. M. Gray, 1982: Tropical cyclone movement and surrounding flow relationship. *Mon. Wea. Rev.,* **110,** 1354–1376.

Charney, J. G., 1955: The use of primitive equations of motion in numerical prediction. *Tellus,* **7,** 22–26.

Chen, J.-H., M. S. Peng, C. A. Reynolds, and C.-C. Wu, 2009: Interpretation of tropical cyclone forecast sensitivity from the singular vector perspective. *J. Atmos. Sci.,* **66,** 3383–3400.

Chen, S.-G., C.-C. Wu, J.-H. Chen, and K.-H. Chou, 2011: Validation and interpretation of adjoint-derived sensitivity steering vector as targeted observation guidance. *Mon. Wea. Rev.,* **139,** 1608–1625.

Chou, K.-H., C.-C. Wu, P.-H. Lin, S. D. Aberson, M. Weissmann, F. Harnisch, and T. Nakazawa, 2011: The impact of dropwindsonde observations on typhoon track forecasts in DOTSTAR and T-PARC. *Mon. Wea. Rev.,* **139,** 1728–1743.

Davis, C. A., 1992: Piecewise potential vorticity inversion. *J. Atmos. Sci.,* **49,** 1397–1411.

DeMaria, M., 1985: Tropical cyclone motion in a nondivergent barotropic model. *Mon. Wea. Rev.,* **113,** 1199–1210.

Elsberry, R. L., and P. A. Harr, 2008: Tropical cyclone structure (TCS08) field experiment science basis, observational platforms, and strategy. *Asia-Pac. J. Atmos. Sci.,* **44,** 209–231.

Fiorino, M., and R. L. Elsberry, 1989: Some aspects of vortex structure related to tropical cyclone motion. *J. Atmos. Sci.,* **46,** 975–990.

Han, J., and H.-L. Pan, 2011: Revision of convection and vertical diffusion schemes in the NCEP Global Forecast System. *Wea. Forecasting,* **26,** 520–533.

Harnisch, F., and M. Weissmann, 2010: Sensitivity of typhoon forecasts to different subsets of targeted dropsonde observations. *Mon. Wea. Rev.,* **138,** 2664–2680.

Hoskins, B. J., M. E. McIntyre, and A. W. Robertson, 1985: On the use and significance of isentropic potential vorticity maps. *Quart. J. Roy. Meteor. Soc.,* **111,** 877–946.

Huang, Y.-H., M. T. Montgomery, and C.-C. Wu, 2012: Concentric eyewall formation in Typhoon Sinlaku (2008). Part II: Axisymmetric dynamical processes. *J. Atmos. Sci.,* **69,** 662–674.

Kunii, M., T. Miyoshi, and E. Kalnay, 2012: Estimating the impact of real observations in regional numerical weather prediction using an ensemble Kalman filter. *Mon. Wea. Rev.,* **140,** 1975–1987.

Kurihara, Y., M. A. Bender, and R. J. Ross, 1993: An initialization scheme of hurricane models by vortex specification. *Mon. Wea. Rev.,* **121,** 2030–2045.

——, ——, R. E. Tuleya, and R. J. Ross, 1995: Improvements in the GFDL hurricane prediction system. *Mon. Wea. Rev.,* **123,** 2791–2801.

Lander, M. A., 1996: Specific tropical cyclone track types and unusual tropical cyclone motions associated with a reverse-oriented monsoon trough in the western North Pacific. *Wea. Forecasting,* **11,** 170–186.

Majumdar, S. J., S.-G. Chen, and C.-C. Wu, 2011: Characteristics of ensemble transform Kalman filter adaptive sampling guidance for tropical cyclones. *Quart. J. Roy. Meteor. Soc.,* **137,** 503–520.

Shapiro, L. J., 1996: The motion of Hurricane Gloria: A potential vorticity diagnosis. *Mon. Wea. Rev.,* **124,** 2497–2508.

——, 1999: Potenial vorticity asymmetries and tropical cyclone motion. *Mon. Wea. Rev.,* **127,** 124–131.

Weissmann, M., and Coauthors, 2011: The influence of dropsondes on typhoon track and midlatitude forecasts. *Mon. Wea. Rev.,* **139,** 908–920.

Wu, C.-C., 2006: Targeted observation and data assimilation in track prediction. *Proc. Sixth Int. Workshop on Tropical Cyclones (IWTC-VI),* WMO TMRP 72, San Jose, Costa Rica, WMO, 409–423.

——, and K. A. Emanuel, 1995a: Potential vorticity diagnostics of hurricane movement. Part I: A case study of Hurricane Bob (1991). *Mon. Wea. Rev.,* **123,** 69–92.

——, and ——, 1995b: Potential vorticity diagnostics of hurricane movement. Part II: Tropical Storm Ana (1991) and Hurricane Andrew (1992). *Mon. Wea. Rev.,* **123,** 93–109.

——, and Y. Kurihara, 1996: A numerical study of the feedback mechanisms of hurricane–environment interaction on hurricane movement from the potential vorticity perspective. *J. Atmos. Sci.,* **53,** 2264–2282.

——, and Y.-H. Kuo, 1999: Typhoons affecting Taiwan: Current understanding and future challenges. *Bull. Amer. Meteor. Soc.,* **80,** 67–80.

——, T.-S. Huang, W.-P. Huang, and K.-H. Chou, 2003: A new look at the binary interaction: Potential vorticity diagnosis of the unusual southward movement of Tropical Storm Bopha (2000) and its interaction with Supertyphoon Saomai (2000). *Mon. Wea. Rev.,* **131,** 1289–1300.

——, ——, and K.-H. Chou, 2004: Potential vorticity diagnosis of the key factors affection the motion of Typhoon Sinlaku (2002). *Mon. Wea. Rev.,* **132,** 2084–2093.

——, and Coauthors, 2005: Dropwindsonde Observations for Typhoon Surveillance near the Taiwan Region (DOTSTAR): An overview. *Bull. Amer. Meteor. Soc.,* **86,** 787–790.

——, J.-H. Chen, P.-H. Lin, and K.-H. Chou, 2007a: Targeted observations of tropical cyclone movement based on the adjoint-derived sensitivity steering vector. *J. Atmos. Sci.,* **64,** 2611–2626.

——, K.-H. Chou, P.-H. Lin, S. D. Aberson, M. S. Peng, and T. Nakazawa, 2007b: The impact of dropwindsonde data on typhoon track forecasts in DOTSTAR. *Wea. Forecasting,* **22,** 1157–1176.

——, and Coauthors, 2009a: Intercomparison of targeted observation guidance for tropical cyclones in the northwestern Pacific. *Mon. Wea. Rev.,* **137,** 2471–2492.

——, S.-G. Chen, J.-H. Chen, K.-H. Chou, and P.-H. Lin, 2009b: Interaction of Typhoon Shanshan (2006) with the midlatitude trough from both adjoint-derived sensitivity steering vector and potential vorticity perspectives. *Mon. Wea. Rev.,* **137,** 852–862.

——, ——, ——, ——, and ——, 2009c: Reply. *Mon. Wea. Rev.,* **137,** 4425–4432.

——, G.-Y. Lien, J.-H. Chen, and F. Zhang, 2010: Assimilation of tropical cyclone track and structure based on the ensemble Kalman filter (EnKF). *J. Atmos. Sci.,* **67,** 3806–3822.

——, Y.-H. Huang, and G.-Y. Lien, 2012: Concentric eyewall formation in Typhoon Sinlaku (2008). Part I: Assimilation of T-PARC data based on the ensemble Kalman filter (EnKF). *Mon. Wea. Rev.,* **140,** 506–527.

Wu, L., and B. Wang, 2000: A potential vorticity tendency diagnostic approach for tropical cyclone motion. *Mon. Wea. Rev.,* **128,** 1899–1911.

——, and ——, 2001: Movement and vertical coupling of adiabatic baroclinic tropical cyclones. *J. Atmos. Sci.,* **58,** 1801–1814.

Yamaguchi, M., T. Iriguchi, T. Nakazawa, and C.-C. Wu, 2009: An observing system experiment for Typhoon Conson (2004) using a singular vector method and DOTSTAR data. *Mon. Wea. Rev.,* **137,** 2801–2816.

Yang, C.-C., and C.-C. Wu, 2010: Potential vorticity diagnosis of the key factors affecting the motion of Typhoon Fengshen (2008)—Why the numerical model prediction fails? Preprints, *29th Conf. on Hurricanes and Tropical Meteorology,* Tucson, AZ, Amer. Meteor. Soc., 663–664.

——, ——, K.-H. Chou, and C.-Y. Lee, 2008: Binary interaction between Typhoons Fengshen (2002) and Fungwong (2002) based on the potential vorticity diagnosis. *Mon. Wea. Rev.,* **136,** 4593–4611.

Zhang, F., Z. Meng, and A. Aksoy, 2006: Tests of an ensemble Kalman filter for mesoscale and regional-scale data assimilation. Part I: Perfect model experiments. *Mon. Wea. Rev.,* **134,** 722–736.